

Self-Organized Ordered Arrays of Core–Shell Columns in Viscous Bilayers Formed by Spatially Varying Electric Fields

P. Dinesh Sankar Reddy,[†] Dipankar Bandyopadhyay,[‡] and Ashutosh Sharma^{*,†}

Department of Chemical Engineering, Indian Institute of Technology Kanpur, 208016, Uttar Pradesh, India and Department of Chemical Engineering, Indian Institute of Technology Guwahati, 781039, Assam, India

Received: July 7, 2010; Revised Manuscript Received: August 26, 2010

A nonlinear analysis is presented to identify the conditions for the formation of ordered patterns consisting of arrays of core–shell columnar structures in thin viscous bilayers by applying a spatially varying electric field. The influence of the electric field strength, film thickness, and topography of the electrode patterns on the order and morphology of the mesostructures is thus investigated. The material with the higher permittivity in the bilayer forms the core, the other one forming the shell. Bilayers under a uniform electric field show only a hexagonal order, whereas a patterned electrode can impose other more complex ordered arrangements, which upon etching of one of the phases produces three-dimensional imbedded hollow structures. Simulations also capture the onset of a phase-inversion phenomenon where the upper layer descends into the lower layer and the latter rises upward to form simple columns without the core–shell structure. When the permittivity of the lower layer is higher (or lower), the columns formed are spatially synchronized with the electrode protrusions (or depressions).

I. Introduction

The instability and dynamics of thin polymer films has been studied extensively in recent times because it holds the potential to generate arrays of self-organized periodic micro/nanostructures useful for fabricating integrated microcircuits,¹ optoelectronic devices,² miniaturized drug delivery components,^{3,4} microfluidic devices,⁵ and superhydrophobic surfaces.^{6–12} The thin unstable polymer film is also a prototype in fundamental studies of intermolecular forces, buckling, friction, dewetting, multilayer adsorption, and phase transition. Recent trends¹³ in miniaturization of devices and patterns indicate a greater role for the methods based on physical self-assembly and self-organization of soft materials. A promising method in this context is the self-organized instability and patterning of thin polymer films under the influence of an external field, such as intermolecular forces^{14–58} and electric field.^{59–84}

Self-organizing ultrathin (<100 nm) polymer films can dewet a flat surface and then self-organize into randomly placed droplets under the influence of intermolecular forces.^{14–28} A number of theoretical^{29–41} and experimental^{42–58} works suggest that the periodicity of the dewetted structures can be controlled if topographic (physical) or chemical patterns are decorated on the solid substrate. In contrast to the dewetting process driven by the material properties that cannot be easily altered, use of an electric field provides a more facile and flexible control on the structure formation where a variety of morphologies such as columns, channels, cavities, and holes can be produced under different conditions.^{59–84} Further, unlike the intermolecular interactions that are effective only in ultrathin (<100 nm) films, electric field can be used also for relatively thick micrometer-sized films. Similar to the dewetting scenario, the electric field induced structures can show long-range order when a spatially

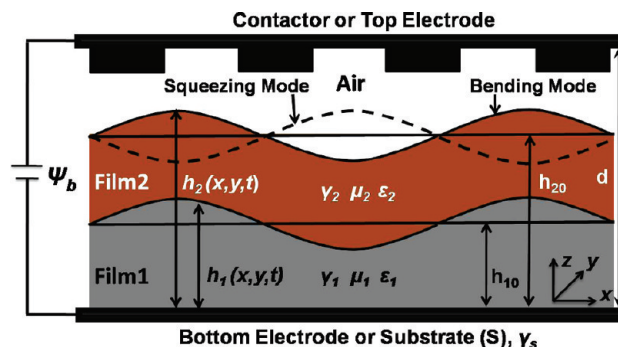


Figure 1. Schematic diagram of a bilayer under the influence of a spatially varying electric field applied by a patterned top electrode and a flat bottom electrode. The mean and local thicknesses of the lower [composite] layer are h_{10} and $h_1(x,y,t)$ [h_{20} and $h_2(x,y,t)$]. The symbols γ_1 , γ_2 , and γ_s represent the surface energies of the lower layer, upper layer, and solid substrate, ϵ_1 , ϵ_2 , and ϵ_s are the relative dielectric permittivities of the lower layer, upper layer, and air, μ_2 and μ_1 denote the viscosities of the upper and lower layer, and d is the distance between the electrodes. The in-phase solid and antiphase dotted line at the upper interface indicate *bending* and *squeezing* modes of evolution with respect to the lower interface. The solid horizontal lines indicate the mean positions of the interfaces.

varying electric field in the form of topographically^{70,75,77,84} or chemically⁸⁴ patterned electrodes is employed.

In contrast to the intermolecular and electric field induced instabilities of a single film where only two-dimensional (2-D) surface structures can be formed, instabilities of thin bilayers^{81–114,118–129} can produce more interesting and difficult to fabricate three-dimensional (3-D) embedded and hollow structures. Figure 1 shows a schematic diagram of a self-organizing bilayer under the influence of an electric field. The instability of a thin bilayer is initiated by either in-phase *bending* or antiphase *squeezing* modes at the two coupled deforming interfaces.⁹⁶ Recent experimental^{81–95} and theoretical^{96–118} studies show some interesting surface patterns engendered by the

* To whom correspondence should be addressed. E-mail: ashutos@iitk.ac.in.

[†] Indian Institute of Technology Kanpur.

[‡] Indian Institute of Technology Guwahati.

instabilities of ultrathin (<100 nm) bilayers under the influence of intermolecular forces. The control of instability by electric field^{119–124} produces an even richer variety of ordered columnar structures in bilayers such as the core–shell and embedded,^{119–121,129} hierarchical,^{122,129} cage-like,¹²⁴ and phase-inverted columnar¹²³ structures. The use of a flat electrode produces only a hexagonal arrangement of columnar structures, so that the use of a patterned electrode is inevitable for engendering any other type of order. Indeed, experiments have shown a facile manipulation of bilayer structures by employing topographically patterned electrodes.¹²² However, theoretical studies^{125–129} of electric field induced instabilities in bilayers have been limited to exploring the pattern formation under a uniform electric field generated by a flat electrode.

In what follows, with the help of 2-D and 3-D nonlinear simulations, we study the ordering of the micro/nanostructures decorated on the two interfaces of viscous bilayers under the influence of spatially varying electric fields. A topographically patterned electrode is employed to impose a periodically varying field that is stronger under the protrusions of the electrode. The role of electrode-pattern periodicity vis-à-vis the natural spinodal length scale of the instability in the bilayer pattern formation is addressed. The influence of the amplitude of the electrode pattern on the morphology and conditions for pattern miniaturization are investigated. The question of which of the two layers organize to form the core or the shell of the composite columns is also investigated. A few recent studies have shown that a bilayer subjected to an electric field can also undergo an interesting phenomenon of phase inversion where the upper layer descends into the lower layer and the latter rises upward to form simple columns without the core–shell structure.^{123,129} The onset of phase inversion is also investigated based on simulations. Finally, the question of synchronization of the columnar structures with the electrode protrusions and depressions is investigated. It is shown that instabilities in the two coupled bilayer interfaces under a spatially varying electric field can engender a variety of ordered, composite microstructures, which can also be transformed in hollow 3-D structures by preferential etching of the core material.

II. Problem Formulation

In this section, we demonstrate the long-wave equations required for the nonlinear simulations of thin viscous bilayer resting on a flat substrate and confined by a patterned electrode from the top. The films are assumed to be dielectric (i.e., materials with a high polarizability), isothermal, and incompressible. Further, Newtonian behavior is assumed because experiments^{122–124} are done well above the glass-transition temperature of the polymer film. We also assume the films to be fully wetting by the short-range effective van der Waals repulsion in order to remove the nonphysical singularity when a contact line appears (local thickness becomes smaller than a few nanometers). For the thicker films considered here, the stronger electric field dominates over the van der Waals force. Figure 1 shows a schematic diagram of such a system. The notations x , y , and z are the coordinates parallel and normal to the substrate, and the symbol t represents time. In the equations shown below the subscript/superscript i denotes the respective layer ($i = 1, 2, s$, and g denote the lower layer, upper layer, solid substrate, and bounding nonviscous gas) and the superscripts denote components of vectors. Thus, for the layer i , $\mathbf{u}^i = \{u_x^i, u_y^i, u_z^i\}$ is the velocity vector, μ_i is the viscosity, ρ_i is the density, γ_i is the surface tension, ε_i is the dielectric permittivity, π_i is the excess pressure because of the externally applied electric

field, $P_i = p_i - \pi_i$ is the effective nonbody force pressure inside the films, and p_i is the isotropic static pressure in the liquid. The subscripts t , x , y , and z denote differentiation with respect to time and the respective coordinate. The variable thicknesses of the bilayer and lower layer are represented by h_2 and h_1 , respectively. Thus, $h_3 = h_2 - h_1$ is the variable thickness of the upper layer. The symbols h_{20} , h_{10} , and h_{30} represent the respective constant base state thicknesses.

A. Nonlinear Equation. The 1-D (one-dimensional) and 2-D (two-dimensional) nonlinear equations for the liquid–liquid and liquid–air interfaces are derived under the following assumptions: (i) the inertial terms are neglected owing to the fact that the films are thin and (ii) the long-wave approximation is valid because all interfacial deformations have small slopes. Starting with the Stokes equations, $\nabla \cdot \bar{\mathbf{T}}^i = \nabla p_i$, and the continuity equation, $\nabla \cdot \mathbf{u}^i = 0$, the kinematic boundary conditions for the individual layers, $\dot{h}_i = -(\mathbf{u}^i \cdot \nabla_s) h_i + \mathbf{u}^i \cdot \mathbf{n}$ at the two interfaces, we obtain the equations for the interfaces, $h_i = h_i(x, y, t)$. The boundary conditions employed for this derivation are $\mathbf{t} \cdot \bar{\mathbf{T}}^2 \cdot \mathbf{n} = 0$ at $z = h_2$ (zero shear at liquid–air interface), $\mathbf{u}^1 = \mathbf{u}^2$, $\mathbf{t} \cdot \bar{\mathbf{T}}^2 \cdot \mathbf{n} = \mathbf{t} \cdot \bar{\mathbf{T}}^1 \cdot \mathbf{n}$ all at $z = h_1$ (continuity of velocity and shear stress at the liquid–liquid interface), and $\mathbf{u}^1 = 0$ at $z = 0$ (no-slip and impermeability at the solid–liquid interface), where $\bar{\mathbf{T}}^i$ is the stress tensor for the i th layer and the notations $\mathbf{n} [(-h_x, 1)/\sqrt{(1 + h_x^2)}]$ and $\mathbf{t} [(1, h_x)/\sqrt{(1 + h_x^2)}]$ represent the normal and tangent vectors, respectively. The symbols ∇ and ∇_s are the gradient operators. It is important to note here that the same formalism has been used successfully to explain the previous experimental results for a single layer.⁶⁶ Details of the derivation case are provided elsewhere.^{97–100,103} The resulting evolution equations are

$$\frac{\partial h_1}{\partial t} - \nabla \cdot \left[\left(\frac{h_1^3}{3\mu_1} \nabla P_1 \right) + \left(\frac{h_1^2(h_2 - h_1)}{2\mu_1} \nabla P_2 \right) \right] = 0 \quad (1)$$

$$\frac{\partial h_2}{\partial t} - \nabla \cdot \left[\left[\frac{(h_2 - h_1)^3}{3\mu_2} + \frac{(h_2 - h_1)h_1}{\mu_1} \left(h_2 - \frac{h_1}{2} \right) \right] \nabla P_2 + \left[\frac{h_1^2}{2\mu_1} \left(h_2 - \frac{h_1}{3} \right) \right] \nabla P_1 \right] = 0 \quad (2)$$

Equations 1 and 2 describe the stability, dynamics, and morphology of the liquid–liquid and liquid–air interfaces. The effective pressures at the liquid–liquid and liquid–air interfaces are derived from the normal stress balances at the respective interfaces as

$$P_1 = p_2 - \gamma_{21} \nabla^2 h_1 - \pi_1 \quad (3)$$

$$P_2 = p_0 - \gamma_2 \nabla^2 h_2 - \pi_2 \quad (4)$$

Here p_0 is the ambient gas pressure and π_1 and π_2 are the excess pressures resulting from the electric field. The electric field applied across the two electrodes polarizes the polymeric films, which are assumed to be dielectric, resulting in an effective surface charge density because of the shift in positive charges toward the field and negative charges in the opposite direction and hence results in an excess pressure at the deformable polymer interfaces.^{77,129} The capacitance of the composite layer (C) can be expressed as^{59,129}

$$\frac{1}{C} = \frac{1}{C_1} + \frac{1}{C_2} + \frac{1}{C_g}, \text{ where } C_1 = \frac{\varepsilon_0 \varepsilon_1 \bar{A}}{h_1},$$

$$C_2 = \frac{\varepsilon_0 \varepsilon_2 \bar{A}}{(h_2 - h_1)}, \text{ and } C_g = \frac{\varepsilon_0 \bar{A}}{(d - h_2)} \quad (5)$$

Here C_1, C_2 , and C_g represent the capacitances of the lower layer, upper layer, and bounding medium, respectively, \bar{A} represents the area of the flat interfaces, and d is the distance between the electrodes. For a constant voltage ψ , the free energy stored in the capacitor device is^{59,129}

$$\Delta G = \frac{\varepsilon_0 \varepsilon_1 \varepsilon_2 \psi^2}{2} \left[\frac{1}{[(h_1 + h_3)\varepsilon_1[\varepsilon_2 - 1] - h_1[\varepsilon_2 - \varepsilon_1] - \varepsilon_2 \varepsilon_1 d]} \right] + \frac{B_1}{(d - h_1 - h_3)^3} + \frac{B_2}{h_1^3} + \frac{B_3}{h_3^3} \quad (6)$$

Here ε_0 is the permittivity of vacuum. To capture the long-time dynamics for the viscous films and remove the contact-line singularities in the nonlinear analysis we introduce short-range repulsion in eq 6. Here a 'softer' repulsive potential^{12,106,114,115,118} is used for the ease of numerical computations. The excess pressures at the interfaces π_1 and π_2 correspond to derivatives of eq 6 with respect to the respective layer thickness¹²⁹

$$\pi_1 = \frac{\partial(-\Delta G)}{\partial h_1} = - \left[\frac{\varepsilon_0 \varepsilon_1 \varepsilon_2 \psi^2 ([\varepsilon_2 - \varepsilon_1] + \varepsilon_1 [1 - \varepsilon_2])}{2[\varepsilon_1(h_1 + h_3)[\varepsilon_2 - 1] - h_1[\varepsilon_2 - \varepsilon_1] - \varepsilon_2 \varepsilon_1 d]^2} \right] - \frac{3B_1}{(d - h_1 - h_3)^4} + \frac{3B_2}{h_1^4} \quad (7)$$

$$\pi_2 = \frac{\partial(-\Delta G)}{\partial h_3} = - \left[\frac{\varepsilon_0 \varepsilon_1 \varepsilon_2 \psi^2 [1 - \varepsilon_2]}{2[\varepsilon_1(h_1 + h_3)[\varepsilon_2 - 1] - h_1[\varepsilon_2 - \varepsilon_1] - \varepsilon_2 \varepsilon_1 d]^2} \right] - \frac{3B_1}{(d - h_1 - h_3)^4} + \frac{3B_3}{h_3^4} \quad (8)$$

The expressions for B_1 , B_2 , and B_3 in eqs 7 and 8 are obtained by imposing the minimum of the free energy at the equilibrium cutoff distance, l_0 , thus giving the conditions $\pi_1 = \partial(-\Delta G)/\partial h_1 = 0$ at $h_1 = l_0$, at $(d - h_2) = l_0$, and $\pi_2 = \partial(-\Delta G)/\partial h_3 = 0$ at $h_3 = l_0$.^{106,114,115,118,129} The inclusion of short-range repulsion effective only for ultrathin (<5 nm) film thickness does not affect the evolution of relatively thicker films considered here, which is dominated entirely by the electric field force.

Since the top electrode is patterned, the electric field pressures at the interfaces are functions of the film thicknesses and spatial coordinates, $\pi_i = f(x, y, h_1, h_3)$. The gradient of electrical pressures can thus be written in the following manner^{34,115,118}

$$d\pi_i = \frac{\partial \pi_i}{\partial h_1} dx + \frac{\partial \pi_i}{\partial h_3} dh_3 + \frac{\partial \pi_i}{\partial x} dx + \frac{\partial \pi_i}{\partial y} dy \quad (9)$$

Here, $\alpha|_\beta$ implies a variable α evaluated at constant β . The gradients of potentials, ∇P_1 and ∇P_2 , in eqs 1 and 2 include the forces because of the local film thickness variations (the first two terms in eq 9) and also the forces resulting from the imposed spatial heterogeneity of the electric field via its spatial dependence on the surface topography $f(x, y)$ (the last two terms in eq 9). The spinodal instability^{34,115,118} of a spatially homogeneous field is engendered by the force component $(\partial \pi_i / \partial h_i) \nabla h_i$ at a given location, which causes a flow from the thinner to the thicker regions of the film whenever the spinodal parameter is negative. The second force due to the heterogeneity of the electric field moves the fluid from the low to high regions of electric field. For example, the patterned electrode imposes a higher electrical stress at the zones where the air gap is small. Thus, the fluid flows from the regions where the electrode spacing (air gap) is higher to where it is lower. This effect is similar to the movement of a liquid in a thin film from the lower wettability to higher wettability regions on a substrate.²⁹⁻³⁵

B. Solution of the Nonlinear Equations: Numerical Methods. The evolution eqs 1 and 2 are nondimensionalized for a compact representation of numerical results by introducing $X = K^{1/2}(x/h_{10})$; $Y = K^{1/2}(y/h_{10})$; $T = (\gamma_{21} K^2)/(3 \mu_1 h_{10} t)$; $H_1 = h_1/h_{10}$; $H_2 = h_2/h_{10}$; $D = d/h_{10}$; $M = \gamma_2/\gamma_{21}$; $R = \mu_1/\mu_2$; $\bar{P}_1 = P_1 h_{10}/K \gamma_{21}$; $\bar{P}_2 = P_2 h_{10}/K \gamma_{21}$, and $K = (\varepsilon_0 \psi_b^2 / 2 \gamma_{21} h_{10})$

$$H_{1T} - \nabla \cdot [H_1^3 \nabla \bar{P}_1] - \frac{3}{2} \nabla \cdot [H_1^2 (H_2 - H_1) \nabla \bar{P}_2] = 0 \quad (10)$$

$$H_{2T} - \nabla \cdot \left[\frac{3}{2} H_1^2 \left(H_2 - \frac{H_1}{3} \right) \nabla \bar{P}_1 \right] - \nabla \cdot \left[\left[R (H_2 - H_1)^3 + 3 (H_2 - H_1) H_1 \left(H_2 - \frac{H_1}{2} \right) \right] \nabla \bar{P}_2 \right] = 0 \quad (11)$$

Equations 10 and 11 were discretized in space using a central difference scheme with half node interpolation, and the resulting stiff ordinary differential equations in time were solved using Gear's time marching algorithm with the help of the D02NCF subroutine of NAG library. Periodic boundary conditions were applied at the space boundaries. The simulations were initialized with an initial volume preserving random perturbation. The grid independence of the solutions was also performed for the simulations.

III. Results and Discussion

An externally applied electric field generates stresses at the soft deformable interfaces of a bilayer (Figure 1), thus making it unstable to form a number of interesting encapsulated and embedded microstructures.^{122-124,129} The difference in the dielectric permittivity of liquid films can give a first estimate on the degree of deformations at the interfaces. For example, the interface between the upper layer and air always deforms more toward the upper electrode because the larger dielectric permittivity of the upper layer ($\varepsilon_2 > \varepsilon_g$) leads to a larger stress relaxation when columnar structures are formed in the upper layer. In contrast, the interface between the upper and the lower layer can deform either toward the upper electrode when $\varepsilon_1 > \varepsilon_2$ or toward the substrate in the case of $\varepsilon_1 < \varepsilon_2$. Therefore, choice of material plays an important role in fabricating different types of structures employing bilayers.

In a recent study, the interfacial deformation modes of the bilayer under the influence of a uniform electric field with a flat electrode were discussed.¹²⁹ In particular, the basic influences

TABLE 1: Typical Values of Bilayer Parameters^{122–124}

variables	set I	set II
ϵ_0 (C ² /N m ²)	8.85×10^{-12}	8.85×10^{-12}
ψ (V)	50	50
γ_{21} (N/m)	0.0007	0.000015
γ_2 (N/m)	0.03	0.03
μ_2 (Pa s)	1	1
μ_1 (Pa s)	1	1
d (nm)	1000	3000
h_{10} (nm)	150	500
h_{30} (nm)	100	500

of the dielectric permittivities, viscosities, and surface tensions of the films on the morphological evolution were investigated. In what follows, the important role played by a topographically patterned electrode in the formation of ordered structures is demonstrated. The simulations shown in this study have spatial dimension in the multiples of Λ , which is the dimensionless dominant wavelength (spinodal length scale) corresponding to the maximum growth rate of the instability obtained from the linear stability analysis of a bilayer confined between two flat electrodes.¹²⁹ The typical parameter values used for the nonlinear analyses correspond to a few previous experimental works^{122–124} and are listed in Table 1.

Figure 2 shows the nonlinear evolution of a bilayer with $\epsilon_2 > \epsilon_1$ under a 2-D checker-box patterned top electrode with a

pattern periodicity the same as the spinodal length scale Λ . The height of the downward protrusions of the patterns shown in the top electrode is $0.2D$, where D is the dimensionless distance between the electrodes. Figure 2a and 2b and 2d–f shows the 2-D and 3-D temporal evolution, respectively, of the bilayer interfaces. Figure 2c shows the patterned top electrode with a pattern periodicity of Λ and amplitude of $0.2D$. The linear bending mode of deformation at the early stage of evolution forms columnar structures in the upper layer ($\epsilon_2 > \epsilon_g$), raising also some of the underlayer liquid with it [Figure 2a and 2d]. However, in this case with $\epsilon_2 > \epsilon_1$, the later nonlinear stage of evolution forces a downward deformation of the liquid–liquid interface. The columns of the upper liquid at this stage grow downward to reach the substrate and become encapsulated by the lower layer [Figure 2b and 2e]. Thus, as the upper layer columns touch the top electrode and start to form contact zones with it, the lower layer liquid forms beaker-like structures encapsulating the upper layer columns [Figure 2b and 2f]. The inset image in Figure 2 clearly depicts the shape of a single microstructure thus formed. Selective removal of the core material would thus produce hollow columns of the lower layer material. Interestingly, as the top electrode is patterned with either square (Figure 2a) or hemispherical (Figure 2c) protrusions, the microstructures form just underneath the patterns on the electrode where the electric field induced stresses are highest.

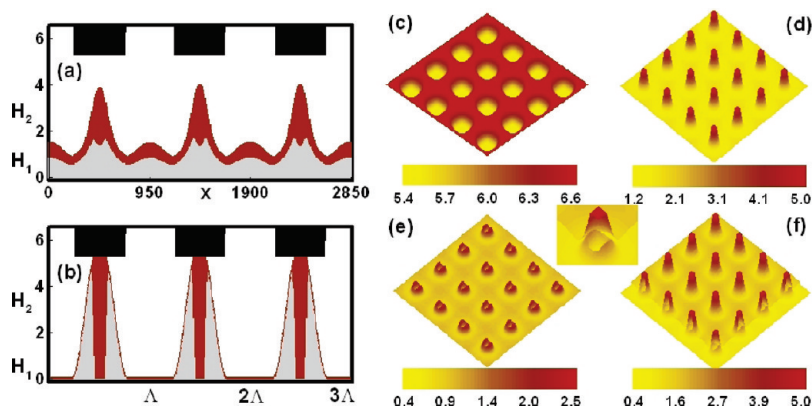


Figure 2. (a and b) 2-D spatiotemporal evolution of the instability in a 3Λ domain. Plot (c) shows the patterns on the top electrode with a pattern periodicity of Λ and amplitude of $0.2D$. Plots (d–f) show 3-D spatiotemporal evolution of the instability of the liquid–air interface, liquid–liquid interface, and composite images, respectively, in a $4\Lambda \times 4\Lambda$ domain when $\epsilon_1 = 2.0$ and $\epsilon_2 = 3.0$. (c) Patterns on the top electrode with a pattern periodicity of Λ and amplitude of $0.2D$. Snapshots of the images given are at times $T =$ (a) 2.49×10^5 , (b) 1.79×10^{15} , and (d–f) 2.62×10^5 . The other parameters are as given in Table 1.

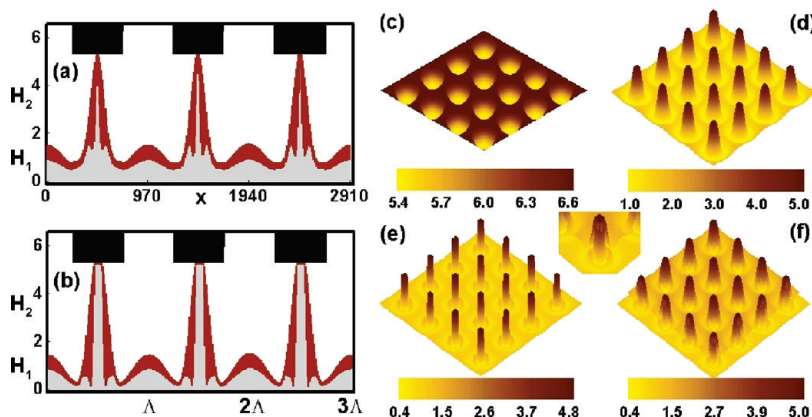


Figure 3. (a and b) 2-D spatiotemporal evolution of the instability in a 3Λ domain. Plot (c) shows the patterns on the top electrode with a pattern periodicity of Λ and amplitude of $0.2D$. Plots (d–f) show 3-D spatiotemporal evolution of the instability of the liquid–air interface, liquid–liquid interface, and composite images, respectively, in a $4\Lambda \times 4\Lambda$ domain when $\epsilon_1 = 3.0$ and $\epsilon_2 = 2.0$. (c) Patterns on the top electrode with a pattern periodicity of Λ and amplitude of $0.2D$. Snapshots of the images given are at times $T =$ (a) 6.8×10^5 , (b) 3.8×10^6 , and (d–f) 4.54×10^5 . The other parameters are as given in Table 1.

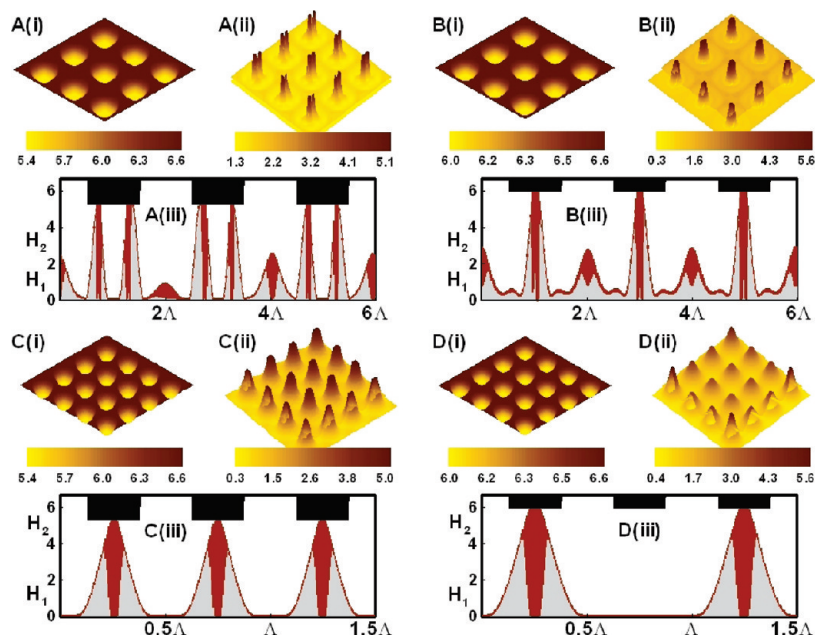


Figure 4. Images A(i)–D(i) show the patterns on the top electrode. Images A(ii)–D(ii) and A(iii)–D(iii) represent 3-D and 2-D interfacial morphologies for a bilayer under patterned electrodes when $\epsilon_1 = 2.0$ and $\epsilon_2 = 3.0$. Images A(i)–D(i) show the patterns on the top electrode. Image sets A and B correspond to the pattern periodicity of 2Λ at the top electrode, whereas image sets C and D correspond to the pattern periodicity of 0.5Λ at the top electrode. The amplitude of patterns on the top electrode for image sets A and C is $0.2D$, and the same for the image sets B and D is $0.1D$. Snapshots of the morphologies given are at times $T = (A(ii)) 4.94 \times 10^5$, $(A(iii)) 1.06 \times 10^9$, $(B(ii)) 1.53 \times 10^6$, $(B(iii)) 1.13 \times 10^7$, $(C(ii)) 2.62 \times 10^5$, $(C(iii)) 6 \times 10^{16}$, $(D(ii)) 1.82 \times 10^6$, and $(D(iii)) 1.24 \times 10^{18}$. The other parameters are as given in Table 1.

Indeed, this particular microstructure is experimentally observed under similar conditions.¹²²

Figure 3 shows the 2-D [Figure 3a and 3b] and corresponding 3-D [Figure 3d–f] nonlinear simulations of a bilayer system similar to the one shown in Figure 2, except that the permittivities of the two layers are now interchanged ($\epsilon_2 < \epsilon_1$). This combination of the dielectric permittivities ($\epsilon_1 > \epsilon_2 > \epsilon_g$) leads to concentric columnar structures with the inner core of the columns now made of the lower layer material encapsulated by the upper layer material, which makes the outer shell. The composite columns grow toward the top electrode. The inset image in Figure 3 clearly depicts the core–shell shape of a single column thus formed. Similar to Figure 2, Figure 3 also shows that the larger electrical stresses due to the smaller air gap below the electrode protrusions [Figure 3c] causes the structures to align precisely to the patterns decorated on the electrode. Thus, Figures 2 and 3 together show that ordered core–shell microarchitectures can be produced in bilayers by employing a topographically patterned top electrode with a periodicity which is approximately commensurate with the spinodal length scale of the instability.

Figures 4 ($\epsilon_2 > \epsilon_1$) and 5 ($\epsilon_2 < \epsilon_1$) show the ordering of the microstructures when the pattern periodicity of the electrode is either much larger (2Λ) or much smaller (0.5Λ) compared to the spinodal length scale, Λ . The figures also show the influence of the height of the protrusions. Figure 4 ($\epsilon_2 > \epsilon_1$) shows the situation when the columns formed by the upper layer are encapsulated by the lower layer. The images in this figure are snapshots of the quasi-equilibrium structures after the interfaces evolve for a long time but before the coalescence of the structures begins with a much slower dynamics. Experimentally, the quasi-equilibrium structures before ripening can be made permanent by quenching, cross-linking, etc., at this stage. Image set A shows that when the pattern periodicity on the top electrode is 2Λ and the height of protrusion is $0.2D$, a pair of columns is formed under each protrusion. The higher field

strength under the protrusions reduces the length scale of instability locally and can thus produce the two columns under each protrusion of width Λ . In contrast, image set B shows that when the height of the protrusion is reduced to $0.1D$ but keeping the same pattern periodicity as in set A, only a single core–shell column is formed under each protrusion. Image sets A and B thus confirm that the pattern periodicity and height of the patterns fabricated on the electrodes can be used to guide the morphology, ordering, and periodicity of the microstructures formed. Further, images (ii) and (iii) in image set C show that when the height of the protrusion is $0.2D$, it is possible to fabricate a single microstructure under each protrusion even when the pattern periodicity is much less (0.5Λ) than the spinodal length scale, Λ . This also opens up the possibility to miniaturize the film patterns by employing the electrodes patterned on a length scale smaller than the spinodal scale. However, when the height of the protrusion is made significantly smaller ($0.1D$) and the pattern periodicity is also much less than the spinodal lengths scale (0.5Λ), a different scenario is observed. Image set D shows that although at the early stages of evolution the interfaces self-organize into a length scale close to the pattern periodicity, only some of the columns fully grow and touch the electrode at later stages of evolution, as shown in image (iii) in set D. In this case, the pattern periodicity decorated on the electrode is not faithfully reproduced on the film interfaces. A loss of order in the microstructures formed can be observed [images (ii) and (iii) in set D]. In summary, a comparison between the image sets C and D suggests that when the pattern periodicity L is less than Λ and the amplitude of the protrusions is sufficiently large, pattern miniaturization on the length scale L becomes possible without the loss of order.

Figure 5 shows the conditions for ordering of the microstructures where the lower layer columns are encapsulated by the upper layer ($\epsilon_2 < \epsilon_1$). This figure also shows similar general observations as obtained in Figure 4. Images (ii) and (iii) of set A show that when the pattern periodicity is 2Λ and the

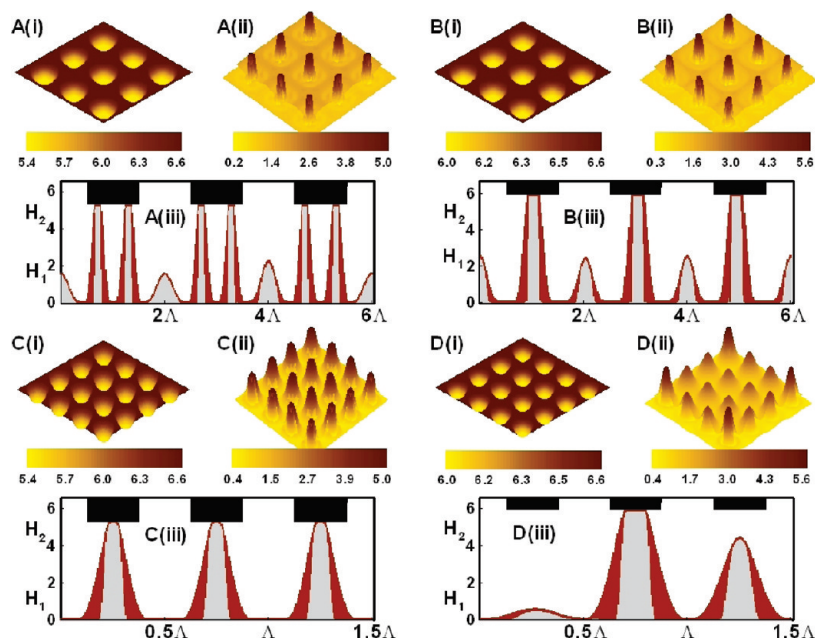


Figure 5. Images A(i)–D(i) show the patterns on the top electrode. Images A(ii)–D(ii) and A(iii)–D(iii) represent 3-D and 2-D interfacial morphologies for a bilayer under patterned electrodes when $\varepsilon_1 = 3.0$ and $\varepsilon_2 = 2.0$. Images A(i)–D(i) show the patterns on the top electrode. Image sets A and B correspond to the pattern periodicity of 2Λ at the top electrode, whereas image sets C and D correspond to the pattern periodicity of 0.5Λ at the top electrode. The amplitude of patterns on the top electrode for image sets A and C is $0.2D$, and the same for the image sets B and D is $0.1D$. Snapshots of the morphologies given are at times $T = (A(ii)) 7.43 \times 10^5$, $(A(iii)) 1.83 \times 10^{10}$, $(B(ii)) 1.8 \times 10^6$, $(B(iii)) 1.62 \times 10^{10}$, $(C(ii)) 4.21 \times 10^5$, $(C(iii)) 1.68 \times 10^{10}$, $(D(ii)) 3 \times 10^6$, and $(D(iii)) 1.05 \times 10^9$. The other parameters are as given in Table 1.

amplitude of the protrusions at the top electrode is $0.2D$, a pair of composite columns are formed under each protrusion. However, only a single structure is observed [images (ii) and (iii) of set B] when the protrusion height is reduced to $0.1D$. Images in set C show that fabrication of miniaturized ordered microstructures with a periodicity less than the spinodal length scale is also possible when the electrode pattern periodicity is less than Λ , and the protrusion height is $0.2D$. However, protrusions with lower amplitude ($0.1D$) can again lead to disorder [image set D].

All previous simulations (Figures 2–5) indicate that the patterns on bilayer films can be fabricated in an ordered manner when a spatially varying electric field is imposed through a patterned electrode. Figure 6 shows the ordering of electric field induced structures when the top electrode is fabricated with a striped pattern [image set A] and the distance between the electrodes is varied. The morphology changes significantly when $\varepsilon_2 > \varepsilon_1$ (image sets B and C) and when $\varepsilon_2 < \varepsilon_1$ (image sets D and E). Image set B depicts that when the distance between electrodes is small ($d = 500$ nm), the upper layer deforms into periodic longitudinal ridges [image (iii)] and exactly replicates the electrode pattern [image (ii) in set A]. The lower layer encapsulates the microstructures formed in the upper layer [image (i)]. This periodic microstructure is also observed in a recent experimental study under similar conditions.¹²² The composite structure fabricated is interesting in many ways. First, the upper layer itself forms ordered periodic microchannels useful for microfluidic or drug delivery devices. Second, the selective etching of the upper layer material from the composite structure would form open microchannels on the surface of the lower layer. These microchannels are much narrower as compared to those formed on the upper layer surface because of the shorter wavelength at the liquid–liquid interface that has lower interfacial tension. Third, by a selective etching of the lower layer material, one can form hollow imbedded microchannels. Further, these structures can be made much more

closely spaced just by increasing the voltage of the electric field and by imposing a smaller electrode periodicity.

Image set C shows that when the distance between the electrodes is increased ($d = 1000$ nm), the composite ridge as shown in image set B now disintegrates in a set of core–shell columns where the core is composed of the upper layer material of higher dielectric permittivity. The distance between the lines of columns is the same as the electrode periodicity. The intercolumn distance along a line is governed by the spinodal length scale as there is no imposed field variation along the stripes. The morphology shown here [image (i)] can lead to an array of cavities if the upper layer is selectively removed. This configuration thus appears attractive for fabricating arrays of micro/nanopots. Image sets D and E investigate the case of when the lower layer has a higher dielectric permittivity, $\varepsilon_2 < \varepsilon_1$. In these cases, a reversal of the materials of the core and shell occurs, namely, the stripes [images (i) and (iii) in set D] and columns [images (i) and (iii) in set E] have the lower layer material in their cores.

A few recent studies have shown that thin bilayers under electric field can also generate phase-inverted structures where the upper layer descends into the lower layer and the latter rises upward to form simple columns without the core–shell structure.^{123,129} Figures 7 and 8 show descending of the top fluid and a rising of the bottom fluid until it forms a surface directly with air rather than a core–shell structure of two fluids as in previous cases. The simulations shown here only capture the initial stages of the phase inversion to the point where further vertical growth of the columns of the lower layer is imminent under the action of field. At this point, the two-layer hydrodynamic model could not be integrated further numerically, which also indicates that the assumption of two distinct interfaces is no longer valid.

It is observed from Figures 7 and 8 that a patterned electrode can direct the alignment of the phase-inverted structures with the electrode topography. Figure 7 shows that when $\varepsilon_2 > \varepsilon_1$ the

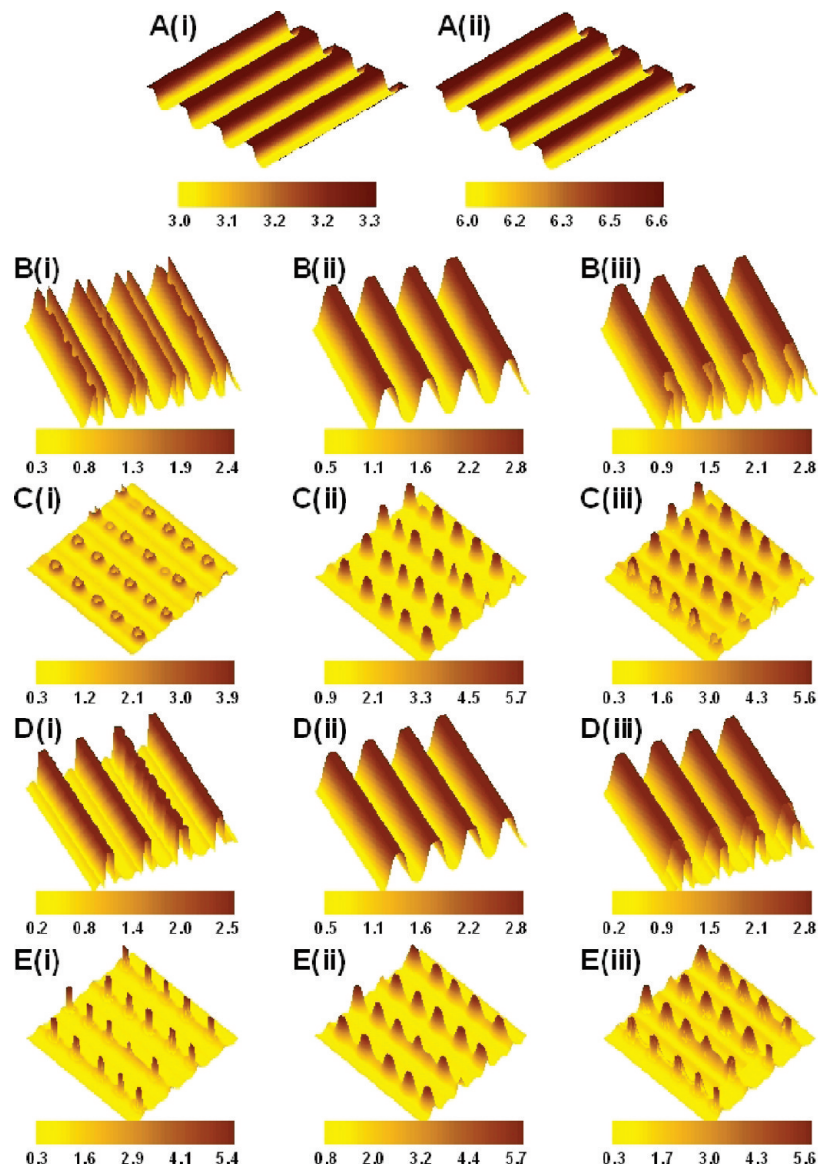


Figure 6. 3-D nonlinear evolutions at the interfaces in a $4\Lambda \times 4\Lambda$ domain. Images (i) and (ii) in set A show the patterns on the top electrode with a pattern periodicity of Λ and amplitude of $0.1d$. Image sets B [D] and C [E] correspond to $\varepsilon_1 = 2.0$ and $\varepsilon_2 = 3.0$ [$\varepsilon_1 = 3.0$ and $\varepsilon_2 = 2.0$] when the spacing between electrodes (d) is 500 and 1000 nm, respectively. Images (i) and (ii) in set A show the patterns on the top electrode with a pattern periodicity of Λ and amplitude of $0.1d$. The Images (i), (ii), and (iii) in rows B–E illustrate the liquid–liquid interface, liquid–air interface, and composite images, respectively. Snapshots are given at times $T =$ (B) 8.28×10^4 , (C) 1.49×10^6 , (D) 7.86×10^4 , and (E) 1.95×10^6 . The other parameters are as given in Table 1.

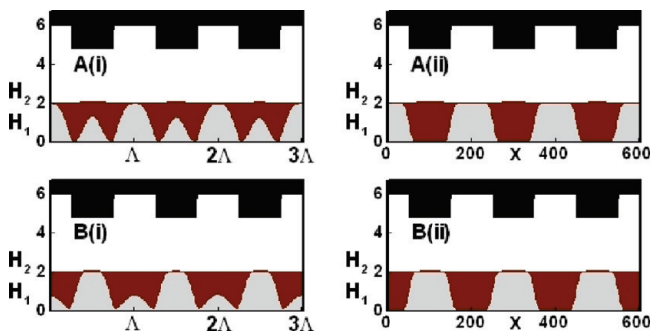


Figure 7. 2-D spatiotemporal evolution of the instability of a set II bilayer in a 3Λ domain when the amplitude of the top electrode pattern is $0.2d$ and periodicity is Λ . Image set A shows the evolution when $\varepsilon_1 = 2.0$ and $\varepsilon_2 = 5.5$, whereas image set B corresponds to $\varepsilon_1 = 5.5$ and $\varepsilon_2 = 2.0$. Snapshots are given at times $T =$ (A(i)) 2.52×10^6 , (A(ii)) 9.5×10^8 , (B(i)) 2.13×10^6 , and (B(ii)) 3.0×10^8 . The other parameters are as given in Table 1.

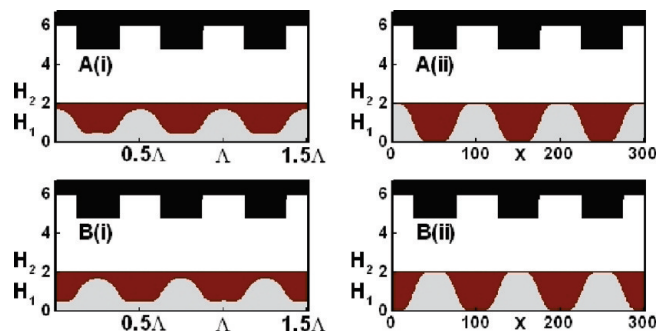


Figure 8. 2-D spatiotemporal evolution of the instability of a set II bilayer in a 1.5Λ domain when the amplitude of top electrode pattern is $0.2d$ and periodicity is 0.5Λ . Image set A shows the evolution when $\varepsilon_1 = 2.0$ and $\varepsilon_2 = 5.5$, whereas image set B corresponds to $\varepsilon_1 = 5.5$ and $\varepsilon_2 = 2.0$. Snapshots are given at times $T =$ (A(i)) 1.41×10^5 , (A(ii)) 1.27×10^8 , (B(i)) 1.3×10^5 , and (B(ii)) 9.66×10^7 . The other parameters are as given in Table 1.

lower layer breaks through the upper layer exactly at the locations that are in phase with the locations of depressions on

the electrode [image set A]. In contrast, in a bilayer with $\varepsilon_2 < \varepsilon_1$ incipient columns of the lower layer form under the

protrusions of the electrode [image set B]. Figure 8 shows that when the periodicity of the electrode pattern is much less (0.5 Λ) than the spinodal length scale, the phase-inversion phenomenon follows a similar pathway as observed in Figure 7. Thus, miniaturized phase-inverted structures with periodicity substantially less than the spinodal length scale are also possible by employing an electrode with finer features.

IV. Conclusions

The conditions for the formation of ordered core–shell and phase-inverted columnar structures in viscous bilayers under the influence of spatially varying electric field are uncovered by 2-D and 3-D nonlinear simulations. The major conclusions are as follows.

(i) Under the influence of an electric field, thin bilayers form an array of core–shell columnar structures where the material with higher (lower) dielectric permittivity constitutes the core (shell), as also observed experimentally.¹²² When the applied field is uniform, only hexagonally ordered structures are formed as also seen experimentally.¹²² However, other more complex arrangements of the composite columns are obtained under spatially varying electric fields. The patterns fabricated on the electrode enforce a lateral variation of the electric field and causes a directed movement of the liquids toward the higher intensity of the field, which eventually causes the ordering of the structures.

(ii) A number of examples are shown where ordered micro-patterns such as the parallel core–shell cylinders or arrays of composite columns are formed by changing the film thickness and electrode topography. The core–shell stripes and columns could be turned into hollow embedded microchannels and micropots when the core material is selectively etched.

(iii) Change in protrusion amplitude and periodicity of the patterns on the top electrode can lead to order and disorder of the microstructures. Small amplitude protrusions with a larger air gap impose a weaker variation in the electric field leading to loss of ordering especially when the pattern periodicity is less than the spinodal wavelength ($L < \Lambda$). However, when the amplitude is large, a much stronger electric field intensity under the electrodes helps in producing ordered patterns even when $L < \Lambda$. This also opens up a pathway for pattern miniaturization by employing patterned electrodes.

(iv) Simulations also capture the onset of phase-inversion phenomenon where the upper layer descends into the lower layer and the lower layer simultaneously breaks through the upper layer to form simple columns. Under a spatially varying electric field, the lower layer columns break through the upper layer exactly at the locations that are in phase with the depressions of the electrode when the upper layer has higher dielectric permittivity ($\epsilon_2 > \epsilon_1$). In contrast, when $\epsilon_2 < \epsilon_1$, the lower layer form incipient columns under the protrusions of the electrode. Thus, the location of phase inversion can also be directed employing a patterned electrode. Interestingly, the growth of columns during phase inversion follows the electrode patterns even when the pattern periodicity at the top electrode is much less than the spinodal length scale ($L < \Lambda$).

The results shown here indicate that bilayers with different materials can be patterned with large-area order and periodicity. This approach can be extended to fabricate multiscale hierarchical structures consisting of a number of different phases/materials with multiple lateral length scales.

Acknowledgment. This work was supported by the DST, New Delhi through an IRHPA grant.

References and Notes

- (1) Hu, Z.; Tian, M.; Nysten, B.; Jonas, A. M. *Nat. Mater.* **2008**, *8*, 62.
- (2) Nie, Z.; Kumacheva, E. *Nat. Mater.* **2008**, *7*, 277.
- (3) Langer, R.; Tirrell, D. A. *Nature* **2004**, *428*, 487.
- (4) Jeong, K. H.; Kim, J.; Lee, L. P. *Science* **2006**, *312*, 557.
- (5) Squires, T. M.; Quake, S. R. *Rev. Mod. Phys.* **2005**, *77*, 977.
- (6) Ball, P. *Nature* **1999**, *400*, 507.
- (7) Nakajima, A.; Hashimoto, K.; Watanabe, T. *Monatsh. Chem.* **2001**, *132*, 31.
- (8) Lafuma, A.; Quéré, D. *Nat. Mater.* **2003**, *2*, 457.
- (9) Blossey, R. *Nat. Mater.* **2003**, *2*, 301.
- (10) van der Wal, P.; Steiner, U. *Soft Matter* **2007**, *3*, 426.
- (11) Li, X.-M.; Reinholdt, D.; Crego-Calama, M. *Chem. Soc. Rev.* **2007**, *36*, 1350.
- (12) Stuart, M. A. C.; Huck, W. T. S.; Genzer, J.; Müller, M.; Ober, C.; Stamm, M.; Sukhorukov, G. B.; Szleifer, I.; Tsukruk, V. V.; Urban, M.; Winnik, F.; Zauscher, S.; Luzinov, I.; Minko, S. *Nat. Mater.* **2010**, *9*, 101.
- (13) Yang, J. K. W.; Jung, Y. S.; Chang, J.; Mickiewicz, R. A.; Alexander-Katz, A.; Ross, C. A.; Berggren, K. K. *Nat. Nanotechnol.* **2010**, *5*, 256.
- (14) Ruckenstein, E.; Jain, R. K. *J. Chem. Soc., Faraday Trans. 2* **1974**, *70*, 132.
- (15) De Gennes, P. G. *Rev. Mod. Phys.* **1985**, *57*, 827.
- (16) Reiter, G. *Phys. Rev. Lett.* **1992**, *68*, 75.
- (17) Brochard-Wyart, F.; Martin, P.; Redon, C. *Langmuir* **1993**, *9*, 3682.
- (18) Sharma, A. *Langmuir* **1993**, *9*, 861.
- (19) Reiter, G. *Langmuir* **1993**, *9*, 1344.
- (20) Oron, A.; Davis, S. H.; Bankoff, S. G. *Rev. Mod. Phys.* **1997**, *69*, 931.
- (21) Sharma, A.; Khanna, R. *Phys. Rev. Lett.* **1998**, *81*, 3463.
- (22) Ghatak, A.; Khanna, R.; Sharma, A. *J. Colloid Interface Sci.* **1999**, *212*, 483.
- (23) Oron, A.; Bankoff, S. G. *J. Colloid Interface Sci.* **1999**, *218*, 152.
- (24) Thiele, U.; Velarde, M.; Neuffer, K. *Phys. Rev. Lett.* **2001**, *87*, 016104.
- (25) Sharma, A.; Mittal, J. *Phys. Rev. Lett.* **2002**, *89*, 186101.
- (26) Narsimhan, G. *J. Colloid Interface Sci.* **2005**, *287*, 624.
- (27) Yang, M. H.; Hou, S. Y.; Chang, Y. L.; Yang, A. C.-M. *Phys. Rev. Lett.* **2006**, *96*, 066105.
- (28) Xu, L.; Shi, T. F.; An, L. J. *Langmuir* **2007**, *23*, 9282.
- (29) Konnur, R.; Kargupta, K.; Sharma, A. *Phys. Rev. Lett.* **2000**, *84*, 931.
- (30) Zope, M.; Kargupta, K.; Sharma, A. *J. Chem. Phys.* **2001**, *114*, 7211.
- (31) Kargupta, K.; Sharma, A. *Phys. Rev. Lett.* **2001**, *86*, 4536.
- (32) Kargupta, K.; Sharma, A. *J. Chem. Phys.* **2002**, *116*, 3042.
- (33) Kargupta, K.; Sharma, A. *Langmuir* **2003**, *19*, 5153.
- (34) Kargupta, K.; Sharma, A. *J. Colloid Interface Sci.* **2002**, *245*, 99.
- (35) Kargupta, K.; Sharma, A. *Langmuir* **2002**, *18*, 1893.
- (36) Brusch, L.; Kühne, H.; Thiele, U.; Bär, M. *Phys. Rev. E* **2002**, *66*, 011602.
- (37) Thiele, U.; Brusch, L.; Bestehorn, M.; Bär, M. *Eur. Phys. J. E* **2003**, *11*, 255.
- (38) Kao, J. C. T.; Golovin, A. A.; Davis, S. H. *J. Colloid Interface Sci.* **2006**, *303*, 532.
- (39) Simmons, D.; Chauhan, A. *J. Colloid Interface Sci.* **2006**, *295*, 472.
- (40) Saprykin, S.; Trevelyan, P. M. J.; Koopmans, R. J.; Kalliadasis, S. *Phys. Rev. E* **2007**, *75*, 026306.
- (41) Lenz, R. D.; Kumar, S. *J. Fluid Mech.* **2007**, *571*, 33.
- (42) Reiter, G.; Auroy, P.; Auvray, L. *Macromolecules* **1996**, *29*, 2150.
- (43) Mayer, E.; Braun, H. G. *Macromol. Mat. Eng.* **2000**, *276/277*, 44.
- (44) Sehgal, A.; Ferreira, V.; Douglas, J. F.; Amis, E. J.; Karim, A. *Langmuir* **2002**, *18*, 7041.
- (45) Zhang, Z.; Wang, Z.; Xing, R.; Han, Y. *Surf. Sci.* **2003**, *539*, 129.
- (46) Wunnicke, O.; Müller-Buschbaum, P.; Wolkenhauer, M.; Lorenz-Haas, C.; Cubitt, R.; Leiner, V.; Stamm, M. *Langmuir* **2003**, *19*, 8511.
- (47) Wang, X.; Ostblom, M.; Johansson, T.; Inganäs, O. *Thin Solid Films* **2004**, *449*, 125.
- (48) Luo, C.; Xing, R.; Han, Y. *Surf. Sci.* **2004**, *552*, 139.
- (49) Zhang, X.; Xie, F.; Tsui, O. K. C. *Polymer* **2005**, *46*, 8416.
- (50) Kim, D. H.; Kim, M. J.; Park, J. Y.; Lee, H. H. *Adv. Funct. Mat.* **2005**, *15*, 1445.
- (51) Mukherjee, R.; Gonuguntla, M.; Sharma, A. *J. Nanosci. Nanotechnol.* **2007**, *7*, 2069.
- (52) Kwon, S. J. *J. Appl. Phys.* **2006**, *99*, 063503.
- (53) Wei, J. H.; Coffey, D. C.; Ginger, D. *J. Phys. Chem. B* **2006**, *110*, 24324.

- (54) Baralia, G. G.; Filiatre, C.; Nysten, B.; Jones, A. M. *Adv. Mater.* **2007**, *19*, 4453.
- (55) Martin, C. P.; Blunt, M. O.; Pauliac-Vaujour, E.; Stannard, A.; Moriarty, P. *Phys. Rev. Lett.* **2007**, *99*, 116103.
- (56) Julthongpipit, D.; Zhang, W. H.; Douglas, J. F.; Karim, A.; Fasolka, M. J. *Soft Matter* **2007**, *3*, 613.
- (57) Berry, B. C.; Stafford, C. M.; Pandya, M.; Lucas, L. A.; Karim, A.; Fasolka, M. J. *Rev. Sci. Instrum.* **2007**, *78*, 072202.
- (58) Mukherjee, R.; Bandyopadhyay, D.; Sharma, A. *Soft Matter* **2008**, *4*, 2086.
- (59) Schäffer, E.; Thurn-Albrecht, T.; Russell, T. P.; Steiner, U. *Nature (London)* **2000**, *403*, 874.
- (60) Schäffer, E.; Thurn-Albrecht, T.; Russell, T. P.; Steiner, U. *Europhys. Lett.* **2001**, *53*, 518.
- (61) Deshpande, P.; Sun, X.; Chou, S. Y. *Appl. Phys. Lett.* **2001**, *79*, 1688.
- (62) Xu, T.; Hawker, C. J.; Russell, T. P. *Macromolecules* **2003**, *36*, 6178.
- (63) Xiang, H.; Lin, Y.; Russell, T. P. *Macromolecules* **2004**, *37*, 5358.
- (64) Leach, K. A.; Lin, Z.; Russell, T. P. *Macromolecules* **2005**, *38*, 4868.
- (65) Harkema, S.; Steiner, U. *Adv. Funct. Mater.* **2005**, *15*, 2016.
- (66) Voicu, N. E.; Harkema, S.; Steiner, U. *Adv. Funct. Mater.* **2006**, *16*, 926.
- (67) Wu, N.; Pease, L. F., III; Russel, W. B. *Adv. Funct. Mater.* **2006**, *16*, 1992.
- (68) Bae, J.; Glogowski, E.; Gupta, S.; Chen, W.; Emrick, T.; Russell, T. P. *Macromolecules* **2008**, *41*, 2722.
- (69) Voicu, N. E.; Ludwigs, S.; Steiner, U. *Adv. Funct. Mater.* **2008**, *20*, 3022.
- (70) Wu, N.; Russel, W. B. *Nano Today* **2009**, *4*, 180.
- (71) Herminghaus, S. *Phys. Rev. Lett.* **1999**, *83*, 2359.
- (72) Pease, L. F., III; Russel, W. B. *J. Chem. Phys.* **2003**, *118*, 3790.
- (73) Pease, L. F., III; Russel, W. B. *Langmuir* **2004**, *20*, 795.
- (74) Wu, N.; Russel, W. B. *Appl. Phys. Lett.* **2005**, *86*, 241912.
- (75) Wu, N.; Pease, L. F., III; Russel, W. B. *Langmuir* **2005**, *21*, 12290.
- (76) Wu, X. F.; Dzenis, Y. A. *J. Phys. D: Appl. Phys.* **2005**, *38* (16), 2848.
- (77) Verma, R.; Sharma, A.; Kargupta, K.; Bhaumik, J. *Langmuir* **2005**, *21*, 3710.
- (78) Kim, D.; Lu, W. *Phys. Rev. B* **2006**, *73*, 035206.
- (79) Arun, N.; Sharma, A.; Shenoy, V.; Narayan, K. S. *Adv. Mater.* **2006**, *18*, 660.
- (80) Tomar, G.; Shankar, V.; Sharma, A.; Biswas, G. *J. Non-Newtonian Fluid Mech.* **2007**, *143*, 120.
- (81) John, K.; Hänggi, P.; Thiele, U. *Soft Matter* **2008**, *4*, 1183.
- (82) Sarkar, J.; Sharma, A.; Shenoy, V. *Phys. Rev. E* **2008**, *77*, 031604.
- (83) Arun, N.; Sharma, A.; Pattader, P. S. G.; Banerjee, I.; Dixit, H. M.; Narayan, K. S. *Phys. Rev. Lett.* **2009**, *102*, 254502.
- (84) Srisvastava, S.; Reddy, P. D. S.; Wang, C.; Bandyopadhyay, D.; Sharma, A. *J. Chem. Phys.* **2010**, *132*, 174703.
- (85) Higgins, A. M.; Jones, R. A. L. *Nature* **2000**, *404*, 476.
- (86) Lambooy, P.; Phelan, K. C.; Haugg, O.; Krausch, G. *Phys. Rev. Lett.* **1996**, *76*, 1110.
- (87) Pan, Q.; Winey, I. K.; Hu, H. H.; Composto, R. J. *Langmuir* **1997**, *13*, 1758.
- (88) Segalman, R. A.; Green, P. F. *Macromolecules* **1999**, *32*, 801.
- (89) Wang, C.; Krausch, G.; Geoghegan, M. *Langmuir* **2001**, *17*, 6269.
- (90) Kang, H.; Lee, S. H.; Kim, S.; Char, K. *Macromolecules* **2003**, *36*, 8579.
- (91) Wunnicke, O.; Müller-Buschbaum, P.; Wolkenhauer, M.; Lorenz-Haas, C.; Cubitt, R.; Leiner, V.; Stamm, M. *Langmuir* **2003**, *19*, 8511.
- (92) Julien LeOpolde, S.; Damman, P. *Nat. Mater.* **2006**, *5*, 957.
- (93) Mukherjee, R.; Pangule, R.; Sharma, A.; Tomar, G. *Adv. Funct. Mater.* **2007**, *17*, 2356.
- (94) de Silva, J. P.; Geoghegan, M.; Higgins, A. M.; Krausch, G.; David, M. O.; Reiter, G. *Phys. Rev. Lett.* **2007**, *98*, 267802.
- (95) Paul, R.; Karabiyik, U.; Swift, M. C.; Hottle, J. R.; Esker, A. R. *Langmuir* **2008**, *24*, 4676.
- (96) Maldarelli, C. H.; Jain, R. K.; Ivanov, I. B.; Ruckenstein, E. *J. Colloid Interface Sci.* **1980**, *78*, 118.
- (97) Danov, K. D.; Paunov, V. N.; Alleborn, N.; Raszillier, H.; Durst, F. *Chem. Eng. Sci.* **1998**, *53*, 2809.
- (98) Danov, K. D.; Paunov, V. N.; Stoyanov, S. D.; Alleborn, N.; Raszillier, H.; Durst, F. *Chem. Eng. Sci.* **1998**, *53*, 2823.
- (99) Paunov, V. N.; Danov, K. D.; Alleborn, N.; Raszillier, H.; Durst, F. *Chem. Eng. Sci.* **1998**, *53*, 2839.
- (100) Pototsky, A.; Bestehorn, M.; Merkt, D.; Thiele, U. *Phys. Rev. E* **2004**, *70*, 025201.
- (101) Kumar, S.; Matar, O. K. *J. Colloid Interface Sci.* **2004**, *273*, 581.
- (102) Matar, O. K.; Gkanis, V.; Kumar, S. *J. Colloid Interface Sci.* **2005**, *286*, 319.
- (103) Bandyopadhyay, D.; Gulabani, R.; Sharma, A. *Ind. Eng. Chem. Res.* **2005**, *44*, 1259.
- (104) Pototsky, A.; Bestehorn, M.; Merkt, D.; Thiele, U. *J. Chem. Phys.* **2005**, *122*, 224711.
- (105) Fisher, L. S.; Golovin, A. A. *J. Colloid Interface Sci.* **2005**, *291*, 515.
- (106) Bandyopadhyay, D.; Sharma, A. *J. Chem. Phys.* **2006**, *125*, 054711.
- (107) Pototsky, A.; Bestehorn, M.; Merkt, D.; Thiele, U. *Europhys. Lett.* **2006**, *74*, 665.
- (108) Nepomnyashchy, A. A.; Simanovskii, I. B. *Phys. Fluids* **2006**, *18*, 112101.
- (109) Nepomnyashchy, A. A.; Simanovskii, I. B. *Phys. Fluids* **2006**, *18*, 032105.
- (110) Nepomnyashchy, A. A.; Simanovskii, I. B. *Phys. Fluids* **2007**, *19*, 122103.
- (111) Fisher, L. S.; Golovin, A. A. *J. Colloid Interface Sci.* **2007**, *307*, 203.
- (112) Lenz, R. D.; Kumar, S. *J. Colloid Interface Sci.* **2007**, *316*, 660.
- (113) Tomar, G.; Sharma, A.; Shenoy, V.; Biswas, G. *Phys. Rev. E* **2007**, *76*, 011607.
- (114) Bandyopadhyay, D.; Sharma, A. *J. Phys. Chem. B* **2008**, *112*, 11564.
- (115) Bandyopadhyay, D.; Sharma, A.; Rastogi, C. *Langmuir* **2008**, *24*, 14048.
- (116) Nepomnyashchy, A. A.; Simanovskii, I. B. *J. Fluid Mech.* **2009**, *631*, 165.
- (117) Nepomnyashchy, A. A.; Simanovskii, I. B. *Phys. Rev. Lett.* **2009**, *102*, 164501.
- (118) Bandyopadhyay, D.; Sharma, A. *J. Phys. Chem. C* **2010**, *114*, 2237.
- (119) Lin, Z.; Kerle, T.; Baker, S. M.; Hoagland, D. A.; Schaffer, E.; Steiner, U.; Russell, T. P. *J. Chem. Phys.* **2001**, *114*, 2377.
- (120) Lin, Z. Q.; Kerle, T.; Russell, T. P.; Schäffer, E.; Steiner, U. *Macromolecules* **2002**, *35*, 3971.
- (121) Lin, Z. Q.; Kerle, T.; Russell, T. P.; Schäffer, E.; Steiner, U. *Macromolecules* **2002**, *35*, 6255.
- (122) Morariu, M. D.; Voicu, N. E.; Schäffer, E.; Lin, Z.; Russell, T. P.; Steiner, U. *Nat. Mat.* **2003**, *2*, 48.
- (123) Leach, K. A.; Gupta, S.; Dickey, M. D.; Wilson, C. G.; Russell, T. P. *Chaos* **2005**, *15*, 047506.
- (124) Dickey, M. D.; Gupta, S.; Leach, K. A.; Collister, E.; Wilson, C. G.; Russell, T. P. *Langmuir* **2006**, *22*, 4315.
- (125) Shankar, V.; Sharma, A. *J. Colloid Interface Sci.* **2004**, *274*, 294.
- (126) Craster, R. V.; Matar, O. K. *Phys. Fluids* **2005**, *17*, 032104.
- (127) Li, F.; Ozen, O.; Aubry, N.; Papageorgiou, D. T.; Petropoulos, P. G. *J. Fluid Mech.* **2007**, *583*, 347.
- (128) Roberts, S. A.; Kumar, S. *J. Fluid Mech.* **2009**, *631*, 255.
- (129) Bandyopadhyay, D.; Sharma, A.; Thiele, U.; Reddy, P. D. S. *Langmuir* **2009**, *25*, 9108.
- (130) Israelachvili, J. N. *Intermolecular and Surface Forces*; Academic Press: London, 1992.
- (131) van Oss, C. J.; Chaudhury, M. K.; Good, R. J. *Chem. Rev.* **1988**, *88*, 927.
- (132) Griffiths, D. J. *Introduction to electrodynamics*; Prentice Hall of India Pvt. Ltd.: New Delhi, 1988.

JP106253K